



# Cu<sub>2</sub>O nano-flowers/graphene enabled scaffolding structure catalyst layer for enhanced CO<sub>2</sub> electrochemical reduction

Yucheng Wang<sup>a,1</sup>, Hanhui Lei<sup>a,1</sup>, Shun Lu<sup>b</sup>, Ziming Yang<sup>c</sup>, Ben Bin Xu<sup>a</sup>, Lei Xing<sup>c,\*</sup>, Terence Xiaoteng Liu<sup>a,\*</sup>

<sup>a</sup> Faculty of Engineering and Environment, Northumbria University, Newcastle upon Tyne NE1 8ST, United Kingdom

<sup>b</sup> Department of Agricultural and Biosystems Engineering, South Dakota State University, Brookings, SD 57007, USA

<sup>c</sup> Department of Engineering Science, University of Oxford, Oxford OX1 3PJ, United Kingdom

## ARTICLE INFO

### Keywords:

CO<sub>2</sub> reduction reaction  
Catalyst layer  
Nanoflower  
Graphene  
Modelling

## ABSTRACT

Nanosized Cu<sub>2</sub>O catalysts with precisely controlled bud-to-blooming flower shapes are synthesised using modified polyol method. The evolution of the shape when the catalysts are applied to the gas diffusion electrodes improves the key factors influencing the catalyst layer, e.g. volume porosity and triple-phase boundary contact areas. Numerical and experimental studies revealed increased reactant molar concentration and improved CO<sub>2</sub> mass transfer due to the structural changes, which influenced the electrochemical CO<sub>2</sub> reduction reaction (eCO<sub>2</sub>RR). The fully bloomed Cu<sub>2</sub>O nanoflower catalyst, combined with the two-dimensional (2D) structured graphene sheet, formed a catalyst layer with scaffolding structure that exhibited the highest Faradaic efficiency (FE) of 93.20% towards CO at an applied potential of −1.0 V vs. RHE in 1 M KOH. These findings established the relationship between the catalyst layer properties and mass transfer, based on which we could describe the effect of the structural design of the catalyst layer on the eCO<sub>2</sub>RR performance.

## 1. Introduction

The 'net zero' target act has urged the development of carbon capture and utilisation technologies, including direct carbon capture [1,2], enhanced weathering [3,4], photochemical CO<sub>2</sub> conversion [5,6] and electrochemical reduction [7,8]. The electrochemical conversion of carbon dioxide (CO<sub>2</sub>) has attracted increasing research attention owing to its many advantages, such as moderate reaction temperature, simple reaction setup, and high energy-density fuel products (e.g. CO and formate), and is one of the most efficient methods for large-scale energy storage, chemical production, and transportation systems [8,9]. Moreover, electrochemical CO<sub>2</sub> reduction reaction (eCO<sub>2</sub>RR) is a controllable process, and different products can be obtained by varying the catalyst architecture, electrolyte pH, applied potential, and electrolyser design etc. [10]. The commercialisation of this technology depends on a high-performance, stable catalyst. Significant effort has been made to overcome the challenges faced by catalysts, such as low catalytic activity [11, 12], low selectivity [13,14], and poor durability of the reaction system [15,16], which reduces the reaction efficiency. Inertness of CO<sub>2</sub>

molecules requires high activation potential [17–19], and the low solubility (~35 mM at 298 K, 1 atm) of CO<sub>2</sub> in the electrolyte reduces the CO<sub>2</sub> mass transfer leading to hydrogen evolution reaction (HER) [20–22].

Significant research has been done over the last few decades to design novel electrocatalysts with enhanced Faradaic efficiency (FE) for a desired eCO<sub>2</sub>RR product by controlling catalyst element selection [7], surface morphology [23], particle size [24], crystallisation [25] and architecture [26]. (1) The metallic catalysts for eCO<sub>2</sub>RR with different elemental types afford different products through different reaction routes [15]. The binding energy difference of the \*CO species in metallic electrocatalysts determines the selectivity of main products [27]. Although noble metals, such as Au, Ag, and Pt, exhibit better CO<sub>2</sub> selectivity toward CO than other metallic catalysts under moderate overpotentials [28], their high cost prohibits their commercialisation. Compared to noble metals, Cu has a low price and significant eCO<sub>2</sub>RR activity [8], and is the only metal that yields multiple products, such as CO, formate, methane, ethane, ethylene, ethyne, methanol, ethanol and other C<sub>2</sub>, or even C<sub>3</sub> organic products [29]. The selectivity of Cu-based

\* Corresponding authors.

E-mail addresses: [lei.xing@eng.ox.ac.uk](mailto:lei.xing@eng.ox.ac.uk), [xinglei1314@gmail.com](mailto:xinglei1314@gmail.com) (L. Xing), [terence.liu@northumbria.ac.uk](mailto:terence.liu@northumbria.ac.uk) (T.X. Liu).

<sup>1</sup> These authors contributed equally to this work.

catalysts depends on the catalyst morphology, local pH, overpotential, and electrolyte concentration [9]. Therefore, the reaction conditions should be carefully controlled to enhance the system selectivity. Cu oxide nanoparticles, such as cuprous oxide ( $\text{Cu}_2\text{O}$ ), have attracted significant attention owing to their relatively high reaction activity for the conversion of  $\text{CO}_2$  into  $\text{CO}$ ,  $\text{CH}_4$ , or  $\text{C}_2$  [30, 31] at relatively low applied potentials. (2) The morphology of the catalyst can be tuned to enhance the catalytic reaction efficiency, with specific morphological and electronic characteristics improving the selectivity and activity of  $\text{eCO}_2\text{RR}$ . Hu et al. [32] reported a unique shape of bismuth-based nanosheets on flow-through hollow fibre, with enhanced formate selectivity and activity, up to 85% with current density of  $141 \text{ mA cm}^{-2}$  at  $-1.0 \text{ V}$  vs. RHE. Jiao et al. [33] developed a Pd octahedra catalyst, represents up to 95% FE of  $\text{CO}$  and better reaction activity than Pd cubes.

The  $\text{CO}_2$  mass transfer influences the efficiency of the reaction system. Recently, gas diffusion electrode (GDE) cells have been employed [22,34] for  $\text{eCO}_2\text{RR}$ , where  $\text{CO}_2$  is fed directly through the gas diffusion layer to the catalyst layer surface, with a short diffusion distance for the gaseous reactants to reach the electroactive sites on the catalyst surface [35]. Wang et al. [36] discovered a bilayer porous electrode with directional diffusion of gas molecules onto the catalyst layer and 94% FE to carbonaceous products at  $-1.0 \text{ V}$  vs. RHE and a current density of  $200 \text{ mA cm}^{-2}$ . Dinh et al. [34] developed a polymer-based hydrophobic gas diffusion electrode, which prevents flooding and has a stable catalyst surface on account of the carbon nanoparticles and graphite, and exhibits 70% FE towards ethylene at  $-0.55 \text{ V}$  vs. RHE. Although the effects of the electrode structure and catalyst layer have been reported, the effects of reduced mass transfer, porosity, and hydrophobicity of the catalyst-coated electrode on the performance have not yet been studied.

A high-performance catalyst with considerable  $\text{CO}_2$  mass transfer is required for an effective reaction system. In this study, we synthesised a series of  $\text{Cu}_2\text{O}$ /graphene (CG) nanoflower composite catalysts with precise bud-to-blooming flower opening degrees. The degree of opening increases at each  $5^\circ\text{C}$  along with temperature increase in synthesis temperature from  $70$  to  $90^\circ\text{C}$  for each catalyst (Fig. 1). The catalysts were printed on GDE as cathode catalyst layers and assembled in a 3D-printed cell to study the effect of the induced mass transfer. The fully bloomed nanoflower forms a scaffolding structure with the graphene sheets (Fig. 1b), and one such structure was assembled as the CG electrode. This resulted in a change in the catalyst layer porosity (Fig. 1c, orange middle layer), and the blooming flower petals increased the exposure of  $\text{Cu}_2\text{O}$  active sites compared to the buds resulting in an

improved surface/volume ratio.

## 2. Experimental

### 2.1. Reagents

All the reagents were of analytical grade and were used without further purification. Copper (II) sulphate pentahydrate ( $\text{CuSO}_4 \cdot 5\text{H}_2\text{O}$ , Sigma-Aldrich) was used as the copper precursor to prepare the catalyst. Graphene powder was purchased from Goodfellow. Ethylene glycol ( $\text{C}_2\text{H}_6\text{O}_2$ ) was purchased from Fisher Scientific (U.K.). Polyvinylpyrrolidone (powder, wt. 10000) and L-ascorbic acid (powder) were purchased from Sigma Aldrich.

### 2.2. Catalyst synthesis

The CG catalysts were synthesised using a modified polyol method. Initially,  $53.5 \text{ mg}$  of graphene,  $150 \text{ mg}$  of L-ascorbic acid (99%, in  $20 \text{ mL}$  deionised water) solution, and  $80 \text{ mL}$  ethylene glycol were mixed in a beaker and sonicated at  $25^\circ\text{C}$  for  $30 \text{ min}$  to remove any oxide formed on graphene. The suspension was transferred into a three-neck flask, and  $200 \text{ mL}$  of ethylene glycol was added. Subsequently, polyvinylpyrrolidone ( $50 \text{ mg}$ ) was dissolved in  $50 \text{ mL}$  of deionised water and added to the flask. After that,  $200 \text{ mg}$  of  $\text{CuSO}_4 \cdot 5\text{H}_2\text{O}$  ( $\text{Cu}:\text{C} = 1:1$  (wt. %)) was dissolved in  $20 \text{ mL}$  of deionised water and added to the flask dropwise. The mixture was then stirred at  $400 \text{ rpm}$  for  $10 \text{ h}$  in  $\text{N}_2$  atmosphere at  $70^\circ\text{C}$ ,  $75^\circ\text{C}$ ,  $80^\circ\text{C}$ ,  $85^\circ\text{C}$ , and  $90^\circ\text{C}$  to obtain flower-like catalysts with different blooming degrees. The suspension was then filtered and washed with ethanol to remove the residual chemicals. A brief schematic of the synthesis procedure is illustrated in Fig. 1a, b, and d. Finally, the as-prepared catalysts were dried in an open-air oven at  $40^\circ\text{C}$ . The catalysts were annotated as CG1, CG2, CG3, CG4, and CG5, corresponding to synthesis temperatures of  $70$ ,  $75$ ,  $80$ ,  $85$ , and  $90^\circ\text{C}$ , respectively. We also synthesised a  $\text{Cu}_2\text{O}$  nanocube catalyst without graphene (which provides a dense catalyst layer for  $\text{eCO}_2\text{RR}$ ) to verify the effect of the catalyst layer structure using a previously reported synthesis method [36].

### 2.3. Physical characterisation

Scanning electron microscopy (SEM), combined with energy-dispersive X-ray spectroscopy (EDX) (MIRA 3, TESCAN at an operating

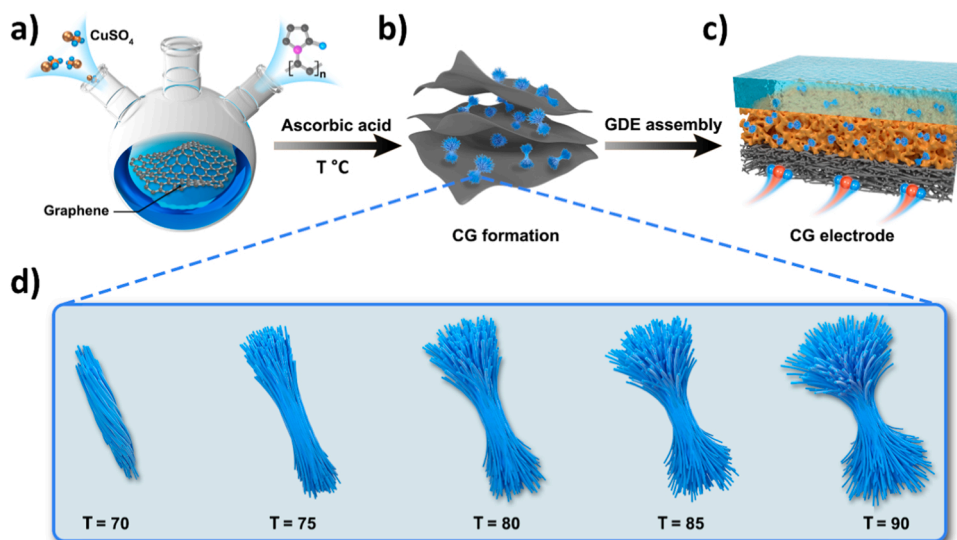


**Fig. 1.** Scheme of CG electrodes for  $\text{eCO}_2\text{RR}$ . (a) Modified polyol method for CG synthesis; (b) CG formation on graphene layer; (c) GDE assembly of CG electrode. (d) Morphology of  $\text{Cu}_2\text{O}$  in CG by controlling the reaction temperature from  $70^\circ\text{C}$  to  $90^\circ\text{C}$ , where  $T$  ( $^\circ\text{C}$ ) represents the synthesis temperature.

voltage of 10 kV), was used to study the morphology and elemental distribution of the catalysts and electrodes. X-ray diffraction (XRD) patterns were obtained on a Rigaku Smartlab II diffractometer with a nominal 3-kW X-ray source to analyse the crystalline structure of the catalysts. An X-ray photoelectron spectroscope (XPS) (SSX-100, Surface Science Laboratories, Inc.), equipped with a monochromatic Al K $\alpha$  X-ray source, was used to characterise the catalyst surface. The CGs were assembled onto carbon paper for the XRD testing, and the CG powders for XPS analysis.

## 2.4. Electrode assembly

The catalyst powder (20 mg) was mixed with 1 mL ethanol in a 2-mL sample tube and sonicated for 10 min. Nafion® solution (40  $\mu$ L; 5 wt.%, Sigma-Aldrich) was added to the tube and sonicated for 1 h. The as-prepared ink was spray-painted onto carbon paper (H23C6, Freudenberg) with an effective surface area of 2 cm<sup>2</sup>. The process was repeated until the mass increased ( $\Delta m$ ) to 5 mg cm<sup>-2</sup>. The catalysts on the gas diffusion layer (GDL) were characterised using SEM/EDS.

## 2.5. Electrochemical evaluation methods

The electrochemical measurements were performed using an Autolab potentiostat/galvanostat (Metrohm Autolab PGSTAT302N). Ag/AgCl and Pt wire were used as the reference and counter electrodes, respectively. The reference electrode was converted to RHE using the following equation:

$$E_{\text{RHE}} = E_{\text{Ag/AgCl}} + 0.197 \text{ V} + 0.0591 \text{ V} \times \text{pH} \quad (1)$$

We studied the electrochemical performance of the catalysts for eCO<sub>2</sub>RR using self-designed GDE-cells, and the full details of our 3D printed device is shown in Fig. S1 in Supplementary Information. A carbon paper GDL served as the current collector and physical substrate for the catalyst; Ag/AgCl and Pt wire were used as the reference and counter electrodes, respectively. CO<sub>2</sub> gas was supplied using a gas inlet into the gas chamber and then diffused across the GDL to reach the catalyst layer. The CO<sub>2</sub> gas flow rate was maintained at 15 mL min<sup>-1</sup> using a flow metre (Cole-Parmer TMR1-010462). The influence of pH on the electrolyte was evaluated at high pH (1 M and 5 M KOH as the catholyte and anolyte, respectively) and moderate pH (1 M and 2 M KHCO<sub>3</sub> as the catholyte and anolyte, respectively). The electrolytes were pre-electrolysed before the electrochemical test using chrono-potentiometry at a constant current density of 3.5 mA cm<sup>-2</sup> using Pt-mesh electrodes for purification. The pre-purge of CO<sub>2</sub> is not required in the electrolyte of the GDE cell. A cation exchange membrane (CEM, Fumapem F-950) was placed between the catholyte and the anode, allowing the cations to transfer through the membrane. The gas products were collected from the gas outlet, and the catholyte was collected for liquid product analysis after the reaction.

To analyse eCO<sub>2</sub>RR behaviour using different catalysts, we performed the chronoamperometry (CA) tests at -0.4 V, -0.6 V, -0.8 V, -1.0 V and -1.2 V vs. RHE for 0.5 h, and measured the current density ( $j$ ) vs. the proceeding time (h). The FE of the electrochemical reaction can be calculated using the input charge and processing time of the electrochemical process in CA, along with the gaseous/liquid product measurement and molar mass calculation. The FEs of the gaseous and liquid products were analysed after 4 h and 8 h of reaction.

To investigate the catalysts' hydrogen evolution reaction (HER) reactivity for the purpose of comprehensively understand the FE results, we performed the linear scanning voltammograms (LSV) at the applied potential range from -0.1 V to -1.4 V vs. RHE at a scan rate of 50 mV s<sup>-1</sup> in 1 M KOH, with N<sub>2</sub> and CO<sub>2</sub> purged conditions, accordingly. The electric double layer capacitance ( $C_{\text{dl}}$ ) of catalysts were estimated by CV scans in the range of -0.1 V to 0.3 V vs. RHE in CO<sub>2</sub> saturated 1 M KOH, at the scan rates from 20 mV s<sup>-1</sup>, 40 mV s<sup>-1</sup>, 60 mV s<sup>-1</sup>, 80 mV s<sup>-1</sup> and

100 mV s<sup>-1</sup> where no Faradaic reaction happens. The double layer capacitances were calculated using the following equation [32, 37]:

$$C_{\text{dl}} = J \left( \frac{dV}{dt} \right) \quad (2)$$

where  $J$  is the current density of 0.1 V vs. RHE, and  $\frac{dV}{dt}$  is the scan rate of CVs.

To evaluate the stability of each catalyst, we performed CA tests in the GDE cell at an applied potential of -1.0 V vs. RHE in 1 M KOH with a constant CO<sub>2</sub> gas supply (15 mL min<sup>-1</sup>). The long-term experiment was conducted for 8 h, and 100 mL catholyte was cycled throughout the reaction.

## 2.6. Products analysis

The gaseous products of eCO<sub>2</sub>RR were collected from the outlet of the reaction cell and analysed using gas chromatography (GC, Shimadzu Tracera GC-2010) coupled with a barrier discharge ionisation detector (BID). The CO<sub>2</sub> flow rate was maintained at 15 mL min<sup>-1</sup> using a flow meter.

The liquid product (formate) was collected from the catholyte and quantified using an ion chromatography (Eco IC, Metrohm) equipped with a 'Metrohm 6.1005.200' column formic acid identification. The FE value for each product was calculated according to Faraday's law [8], and the detailed calculations are provided in the SI.

## 2.7. COMSOL simulation

A multi-physics model based on COMSOL was implemented to investigate the mass transfer and electrochemical reduction of CO<sub>2</sub> at a given flow rate, pressure, temperature, and potential. The model consisted of an electrolyte chamber (EC), catalyst layer (CL), gas diffusion layer (GDL), and gas chamber (GC) (Fig. S2). The fluids through the chambers were assumed to have a laminar flow, and the velocity profile in the porous electrode was described using the Navier-Stokes equation. The calculated gas velocity was correlated with the convective mass transport in the convection-diffusion-reaction equation. The Butler-Volmer equation was used to correlate the relationship between current density and applied electrode potential, and Faraday's law was applied to convert the current density to the generation/consumption rates of chemical species in the system, which were used as the source/sink terms in the convection-diffusion-reaction equation. The concentrations of various species, such as CO<sub>2(g)</sub>, CO<sub>2(aq)</sub>, CO<sub>(g)</sub>, and formate, current and potential distributions, and velocity profiles were correlated, and the hydrogen evolution reaction (HER) was considered as a side reaction. The detailed model development is shown in Fig. S2 and Table S1.

## 2.8. Model assumptions and features

The multi-physics model was developed based on the following assumptions:

- Reactant gas flowing through the cathode channels is treated as laminar flow.
- Sufficient CO<sub>2</sub> was supplied evenly at a constant flow rate at the cathode inlet, and the ideal gas law was applied to the gas species.
- Temperature variation due to chemical reactions is neglected.
- Mass transport occurs through diffusive and convective mechanisms. The Soret effect for mass transport was not considered because of the isothermal assumption.
- The pH of the bulk solution at the anode remained constant, and no acid-base equilibria occurred at the catalyst layer-electrolyte boundary.

- Electrolyte conductivity is independent of the KOH concentration in the studied range.

The model considers the following processes: 1) the conservation of mass, species, charge, and momentum; 2) species transport through the porous electrode under diffusion and convection mechanisms; and 3) species generation and consumption inside the catalyst layer using electrical energy as the driving force. Additionally, the physical properties of the catalyst layer, such as thickness, pore size, and porosity, were also simulated for the catalyst morphology. The governing equations are given by Eqs. 3–10 and Eqs. S3–S11.

## 2.9. Governing equations

The equations describing the conservation of momentum, mass, and species are discussed in the following section. Under the steady-state condition, the continuity equation is applied to describe the mass balance of the reactants flowing through the channel and porous electrode, leading to

$$\nabla \cdot (\rho_g u_g) = 0 \quad (3)$$

where  $\rho_g$  and  $u_g$  are the density and velocity, respectively, of the gas mixture.

For compressive Newtonian fluids, the Navier-Stokes equation is applied to simulate the variation in velocity and pressure within the channel, resulting in

$$\rho_g (u_g \cdot \nabla) u_g = \nabla \cdot \left[ -PI + \mu_g (\nabla u_g + (\nabla u_g)^T) - \frac{2}{3} \mu_g (\nabla \cdot u_g) I \right] + \rho_g g \quad (4)$$

where  $P$  is the pressure,  $I$  is the identity matrix,  $\mu_g$  is the dynamic viscosity of the gas mixture, and  $g$  is the gravitational acceleration. The above equation takes into account the effect of gravity on momentum balance.

The average diffusion model used in COMSOL was selected for species conservation in porous media and gas chambers, and the conservation of species is described by the following diffusion-convection-reaction equation:

$$\nabla \cdot N_i + (u_g \cdot \nabla) c_i = R_i \quad (5)$$

where  $N_i$  is the flux,  $c_i$  is the concentration, and  $R_i$  is the source/sink term of species  $i$ .

The above equation can be re-written as:

$$\nabla \cdot \left( -\rho_g D_{i,m} \nabla \omega_i - \rho_g \omega_i D_{i,m} \frac{\nabla M_g}{M_g} \right) + \nabla \cdot (\rho_g u_g \omega_i) = R_{i,m} \quad (6)$$

where  $\omega_i$  is the mass fraction,  $M_g$  is the mean molar concentration of the gas mixture ( $M_g = (\sum \frac{\omega_i}{M_i})^{-1}$ ),  $M_i$  is the molar concentration of species  $i$ ,  $D_{i,m}$  is the diffusivity of the gas mixture, which comes from the Maxwell-Stefan equation, and is calculated using  $D_{i,m} = \frac{1-\omega_i}{\sum_{k \neq i} \frac{x_k}{D_{ik}}}$ ,  $x_k$  is the molar fraction of gas, and  $D_{ik}$  is the binary diffusivities of the species pairs.

The electrode reaction rate is controlled by charge transfer and is independent of mass transfer when the reactant supply is sufficient. The Tafel equation was chosen as the kinetic expression for the electrode, and the current density was obtained as follows:

$$i_{Ea} = -i_{o,Ea}^{ref} \left( \frac{C_{CO_2(aq)}}{C_{CO_2(aq),Ea}^{ref}} \right) \exp \left[ \frac{\beta_{Ea} F}{R_{ideal} T} (V_0 - V_1 - V_{eq,Ea}^{ref}) \right] \quad (7)$$

$$i_{Eb} = -i_{o,Eb}^{ref} \left( \frac{C_{CO_2(aq)}}{C_{CO_2(aq),Eb}^{ref}} \right) \exp \left[ \frac{\beta_{Eb} F}{R_{ideal} T} (V_0 - V_1 - V_{eq,Eb}^{ref}) \right] \quad (8)$$

$$i_{Ec} = -i_{o,Ec}^{ref} \exp \left( -\frac{\beta_{Ec} F}{R_{ideal} T} (V_0 - V_1 - V_{eq,Ec}^{ref}) \right) \quad (9)$$

where  $i_{o,Ej}^{ref}$  ( $j = a, b, c$ ) are the reference exchange current densities for generating HCOO, CO, and H<sub>2</sub>, respectively,  $C_{CO_2(aq),Ea}^{ref}$  and  $C_{CO_2(aq),Eb}^{ref}$  are the reference concentrations for producing HCOO and CO, respectively,  $R_{ideal}$  is the ideal gas constant;  $\beta_{Ei}$  ( $i = a, b, c$ ) are symmetry factors,  $F$  is the Faraday constant, and  $V_{eq,Ei}^{ref}$  ( $i = a, b, c$ ) are equilibrium potentials.

According to Faraday's law, the electrochemical reaction rates of CO<sub>2</sub>, HCOO, CO, and H<sub>2</sub> can be obtained as follows:

$$R_{E,CO_2(aq)} = \frac{M_{CO_2} a_{sl} (i_{Ea} + i_{Eb})}{2F}; R_{E,HCOO} = -\frac{M_{HCOO} a_{sl} i_{Ea}}{2F};$$

$$R_{E,CO} = -\frac{M_{CO} a_{sl} i_{Eb}}{2F}; R_{E,H_2} = \frac{M_{H_2} a_{sl} i_{Ec}}{2F} \quad (10)$$

where  $M_{CO_2}$ ,  $M_{HCOO}$ ,  $M_{CO}$ , and  $M_{H_2}$  are the molecular weights of each species,  $a_{sl}$  is the specific area of the solid-liquid interface, and an idealised structure of the catalyst layer was designed to calculate the specific area  $a_{sl}$ . The details are presented in Fig. S3. The other equations can be found elsewhere [38].

## 3. Results and discussion

### 3.1. Preparation and characterisation of the catalysts

The SEM morphology and EDS mapping spectra of the catalysts are shown in Fig. 2. With an increase in temperature from 70 °C to 90 °C, the opening degree of the petals increased gradually; it started with nanobuds at 70 °C and developed into nanoflowers at 90 °C. The longitudinal length of CGs range between 1.3 μm and 1.7 μm, and the diameter of each petal is 40 nm. For comparison, the Cu<sub>2</sub>O nanoparticle was characterised (Fig. S4a), and they demonstrated a cubic shape with an average particle size of 100 nm. The EDS mappings of CGs1–5 were studied for elemental analysis (Fig. 2f–o) and indicated an even distribution of Cu and O throughout the nanoparticles.

SEM was used to study the cross-sectional morphology of all the gas diffusion electrodes to calculate the thickness of each CG catalyst layer (Fig. 2p–t). The electrodes were assembled with the same catalyst weight loading and coating area. The thickness of the CG catalysts increased with increasing degree of flower opening, indicating a reduction in the density and increase in the porosity of the catalyst layer with increasing thickness. The catalyst layer of the CGs exhibited a 'sponge' layer rather than a 'compressed layer', and the average thicknesses of CGs1–5 were 38 μm, 42 μm, 50 μm, 56 μm, and 68 μm, respectively. The catalyst layer thickness for the cubic Cu<sub>2</sub>O catalyst was 18 μm (Fig. S4b).

The crystal structure and atomic structure of the CG catalysts were analysed using XRD and XPS (Fig. 3). The XRD pattern of all CG catalysts (Fig. 3a) shows identical characteristic diffraction peaks of Cu<sub>2</sub>O at  $2\theta = 30^\circ, 36^\circ, 42^\circ, 61^\circ, 74^\circ$ , and  $78^\circ$ , corresponding to (110), (111), (200), (220), (311), and (222) planes, respectively; the peak at  $2\theta = 18^\circ$  indicates the PTFE coating on carbon paper (Fig. 3b), while the broad peak at  $2\theta = 25^\circ$  corresponds to graphene. In our experiments, the crystallinity of the catalysts did not influence the CG catalysts performance themselves. To further prove this observation, the average crystallite size was calculated using XRD and shown in Table S2, where all CG catalysts present similar average crystallite size of ca. 31 nm. The XPS Cu 2p spectra of CGs 1–5 are shown in Fig. 3c, where the Cu-related peaks are symmetric. The absence of satellite structure at 943 eV rules out Cu<sup>2+</sup> in the CG catalysts [39]. The two apparent peaks at 933 eV and 953 eV are attributed to the Cu2p3/2 and Cu2p1/2 peaks, respectively, of the Cu<sup>+</sup> in Cu<sub>2</sub>O. The XPS results were consistent for all the catalysts. The XPS survey spectra of CGs 1–5 present a similar pattern (Fig. 3d),



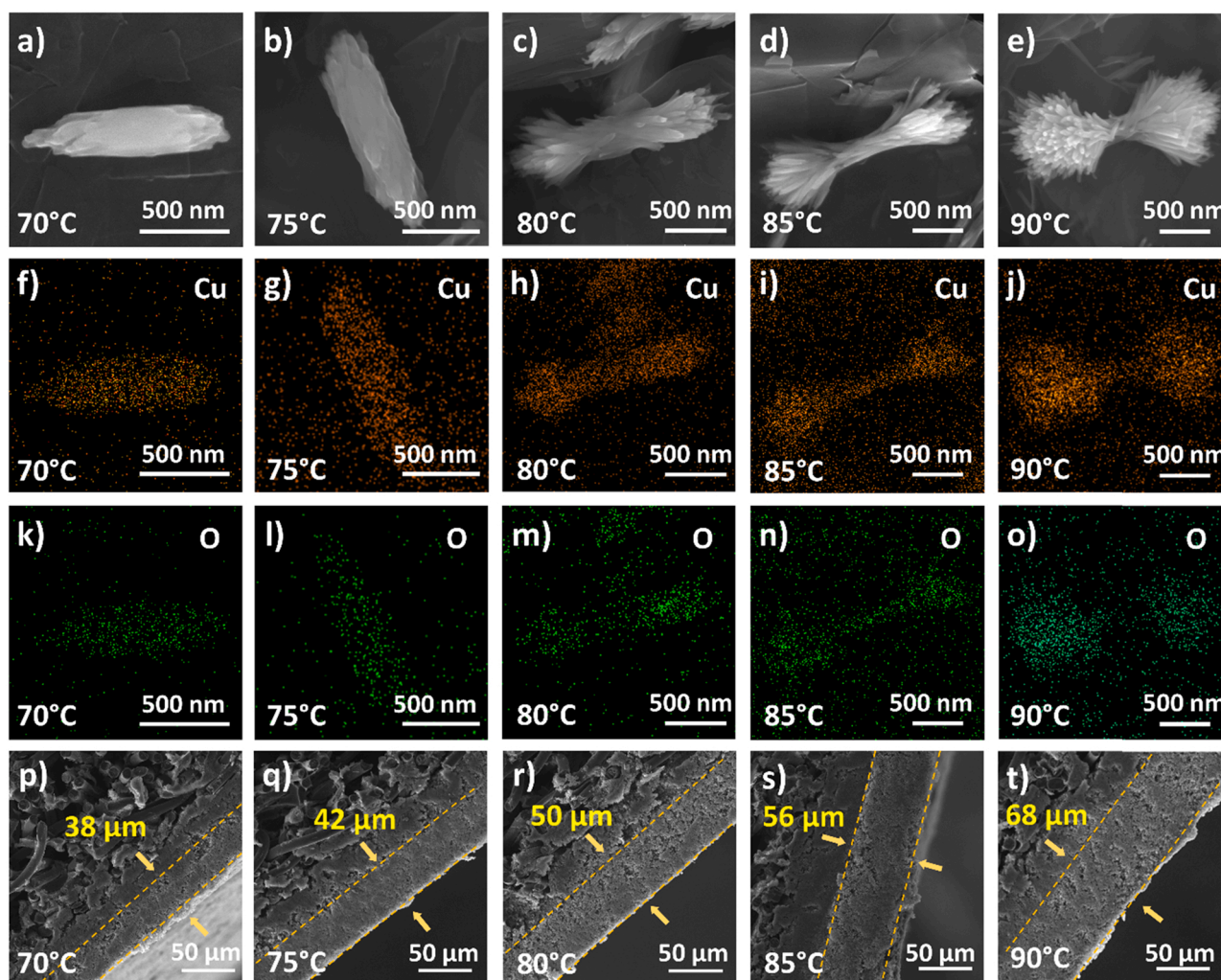


**Fig. 2.** SEM scanning of a–e)  $\text{Cu}_2\text{O}$  nanoparticles on CG1–5 catalysts; EDS mapping of the composition of samples CG1–5; f–j) Cu and k–o) O elemental distribution; p–t) Thickness of catalyst layer via cross-section view of CGs1–5 assembled electrode.

confirming the presence of copper, oxygen, and carbon species. The XRD and XPS results confirmed the similar crystal and atomic structure of these five CG catalysts, indicating that the effect on  $\text{eCO}_2\text{RR}$  performance of CG1–CG5 depends purely on the catalyst morphology-induced catalyst layer property variations.

### 3.2. COMSOL simulation of catalyst layer for $\text{eCO}_2\text{RR}$

The effect of different catalyst layers was simulated to study the properties of CG catalysts for  $\text{eCO}_2\text{RR}$  and to analyse the mass transfer and conversion of  $\text{CO}_2$  gas within the cells. The  $\text{CO}_2$  molar concentrations in the gas chamber and the gas velocity inside the catalyst layers were investigated mathematically using the model developed in COMSOL Multiphysics®.

We calculated the specific interfacial area of each CG catalyst layer, which corresponds to the porosity of each CG catalyst. The pore sizes of the CG catalysts (29, 32, 35, 37, and 40  $\mu\text{m}$  corresponding to CGs1–5, respectively) were calculated using Eqs. S7 and S8 (Fig. 4a). The specific interfacial area exhibited a strong linear relationship with the pore radius. The slope of the linear fitting of the solid-liquid (catalyst layer-electrolyte) interface indicates a minor influence of the pore size of the catalyst layer on the solid-liquid interface. The gas-liquid ( $\text{CO}_2$ -electrolyte) interface improves with increasing pore size, resulting in enhanced mass transfer rate of  $\text{CO}_2$  from the gaseous to aqueous phase owing to the increased contact area between  $\text{CO}_2$  and the electrolyte.

Fig. 4b shows the  $\text{CO}_2$  mass concentration within the GDE cell, and the  $\text{CO}_2$  concentration declines across the top half of the chambers from CG1 to CG5. The CG5 catalyst exhibited the lowest  $\text{CO}_2$  concentration near the outlet of the gas chamber, indicating the highest  $\text{CO}_2$  consumption in CG5. Therefore, CG5 demonstrates the highest mass transfer and reaction efficiency and FE toward CO. The  $\text{CO}_2$  gas velocity in the GDE cell at an applied potential of  $-1.0$  V vs. RHE, corresponding to  $\text{eCO}_2\text{RR}$ , is shown in Fig. 4c.  $X = 0$  indicates the interface between the carbon paper/GDL and catalyst layer, and  $X = 1$  corresponds to the interface between the catalyst layer and gas chamber.  $Y = 0$  and  $Y = 1$  represent the boundaries of the GDL near the gas inlet and outlet, respectively. CG5 exhibited the highest velocity within the GDL on account of its highest porosity. The velocity peaks near  $X = 0.1$  correspond to the partial blockage of the  $\text{CO}_2$  flow due to CL, resulting in velocity loss. The higher velocity near the gas inlet compared to the gas outlet can be attributed to the loss of gas fluid momentum owing to the  $\text{CO}_2$  captured inside the porous electrode, including GDL and CL. The simulation results indicated a linear correlation between the nanoflower opening degree and the porosity and surface/volume ratio. The improved gas velocity indicated enhanced mass transport via a convective mechanism, which accelerated the dissolution of gaseous  $\text{CO}_2$  into the electrolyte and increased the concentration of aqueous  $\text{CO}_2$  resulting in fast  $\text{eCO}_2\text{RR}$  kinetics. The increased specific area changes the internal structure of the catalyst layer by creating more pores that trap the reactant gas ( $\text{CO}_2$ ) within the catalyst layer, forming a robust

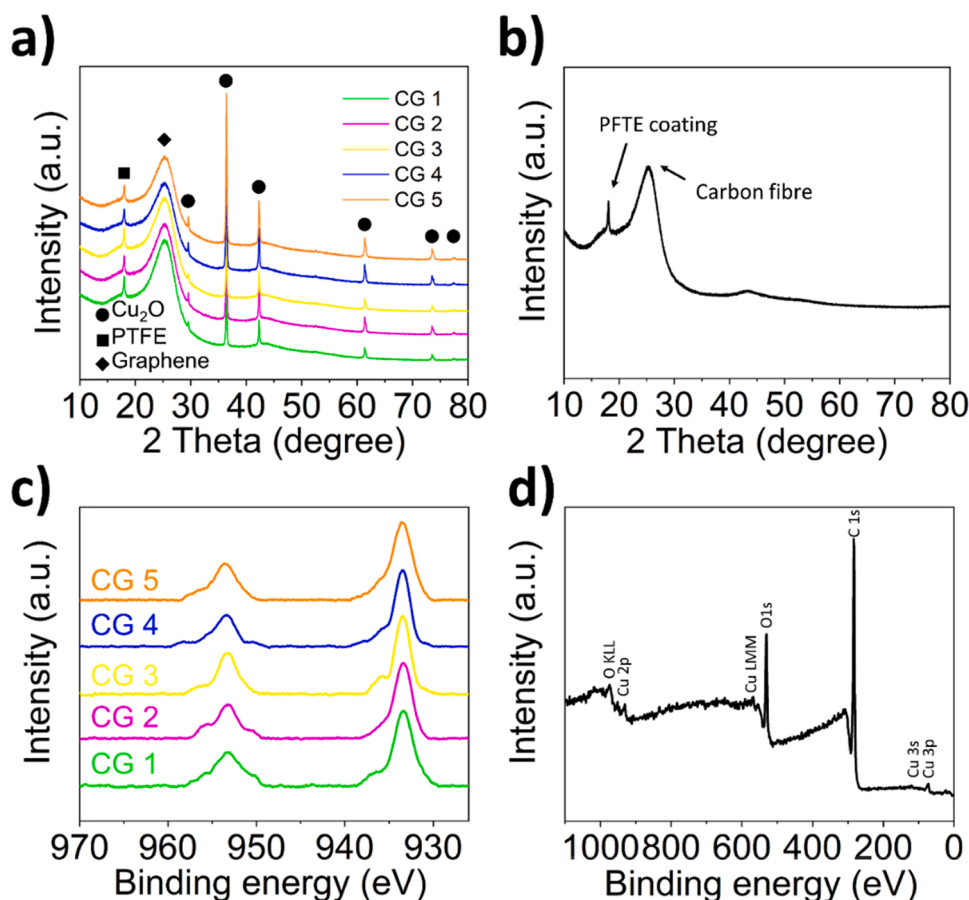


**Fig. 3.** XRD patterns of a) CG electrodes, b) PTFE coated carbon paper as gas diffusion layer, c) XPS spectra of Cu 2p regions of CG catalysts and d) XPS survey spectrum of CG catalysts.

gas-liquid-solid interface for  $\text{eCO}_2\text{RR}$ . Additionally, the porous catalyst also mitigates the GDL flooding [40]. The results indicate higher  $\text{CO}_2$  absorption and higher  $\text{CO}_2$  velocity within the catalyst layer due to the increased specific area and porosity, which improve the  $\text{CO}_2$  reaction and mass transport activity.

### 3.3. Electrochemical $\text{CO}_2$ reduction reaction of CG catalysts in GDE cell

The  $\text{eCO}_2\text{RR}$  properties of all the CG catalysts were evaluated using a GDE cell reaction system, and the FE results of the CG catalysts and  $\text{Cu}_2\text{O}$  cubic nanoparticles in 1 M KOH are shown in Fig. 5. The total current density and  $\text{CO}$  partial current density are shown in Fig. 6, and the detailed data with error analysis are available in Tables S3–S10. The lower FEs for  $\text{CO}$  in the bud-shaped CG1 catalyst correspond to 56.53%, 59.23%, 63.91%, 68.97% and 67.18% at  $-0.4$  V,  $-0.6$  V,  $-0.8$  V,  $-1.0$  V, and  $-1.2$  V vs. RHE, respectively. CG1 also exhibits the lowest current density due to the reduced surface area/volume ratio, which reduces the number of active sites on the surface. The FE and current density of carbonaceous products increase from CG1 to CG5 because of the increase in active sites on the catalyst surface and enhanced porosity of the catalyst layer, which promote the reaction activity and  $\text{CO}_2$  mass transfer. The increased porosity of CG5 resulted in increased surface area of the solid-liquid and gas-liquid interfaces and enhanced the reaction. The FEs at  $-0.4$  V,  $-0.6$  V,  $-0.8$  V,  $-1.0$  V, and  $-1.2$  V vs. RHE are 74.43%, 79.84%, 87.26%, 93.20%, and 91.14%, respectively. The  $\text{Cu}_2\text{O}$  exhibited lower activity and selectivity toward  $\text{eCO}_2\text{RR}$  compared to the CG catalysts. The graphene in the CG catalysts separate the  $\text{Cu}_2\text{O}$  and provides a better gas-liquid-solid interface, thereby promoting charge transfer and  $\text{CO}_2$  mass transfer within the catalyst layer. Contrastingly, pure  $\text{Cu}_2\text{O}$  (Fig. 5f) does not form a porous structure within

the catalyst layers, which reduces the  $\text{CO}_2$  mass transfer and promotes the HER, resulting in poor  $\text{eCO}_2\text{RR}$  [36]. The FEs at  $-0.4$  V,  $-0.6$  V,  $-0.8$  V,  $-1.0$  V, and  $-1.2$  V vs. RHE are 51.07%, 55.98%, 60.80%, 64.85% and 63.31%, respectively. Additionally, the crystal structures also affect the composition of gaseous and liquid products.

To further investigate the performance of CG catalysts in  $\text{eCO}_2\text{RR}$ , we performed LSV for all CG catalysts and  $\text{Cu}_2\text{O}$ . The results are shown in Fig. S5a. In  $\text{N}_2$ -fed condition, all catalysts present a trend of lower current densities at less negative potentials, and gradually increased at higher potentials contributed by HER. While in  $\text{CO}_2$ -fed condition, the current density increases sharply at higher potentials where  $\text{CO}_2\text{RR}$  happens and suppresses the HER. The CG5 presents the highest reaction activity, which agrees well with FE measurement. The statements were confirmed by measuring the double-layer capacitances ( $C_{\text{dl}}$ ) under different scanning rates. As shown in Fig. S5b, the  $C_{\text{dl}}$  of CGs increases from CG1 to CG5, by enhancing their internal porosity, and the  $C_{\text{dl}}$  of CG5 presents over 6 times than that of  $\text{Cu}_2\text{O}$ . It is believed that the presence of graphene allows the nanoflower evenly distributed on the surface and avoid the agglomeration which enhanced its surface active sites. Fig. S5c shows the Tafel parameters of different CGs and  $\text{Cu}_2\text{O}$  for  $\text{eCO}_2\text{RR}$ . All Tafel slopes are lower than  $118 \text{ mV dec}^{-1}$ , which suggests the same mechanism for  $\text{CO}_2$  reduction reaction [32]. With increased porosity and changed morphology of the catalysts, the Tafel plots were decreased from  $82.1 \text{ mV dec}^{-1}$  to  $70.7 \text{ mV dec}^{-1}$ , indicating faster kinetics and higher activity of  $\text{eCO}_2\text{RR}$ .

Above results indicate the synergistic effect between the  $\text{Cu}_2\text{O}$  nanoflower and graphene sheets on the catalyst layer enhances the conversion of  $\text{CO}_2$  to carbonaceous products. Initially, the CG catalyst forms a porous layered structure that enhances the  $\text{CO}_2$  retention and  $\text{CO}_2$  mass transfer. Additionally, the porous catalyst layer enhances the

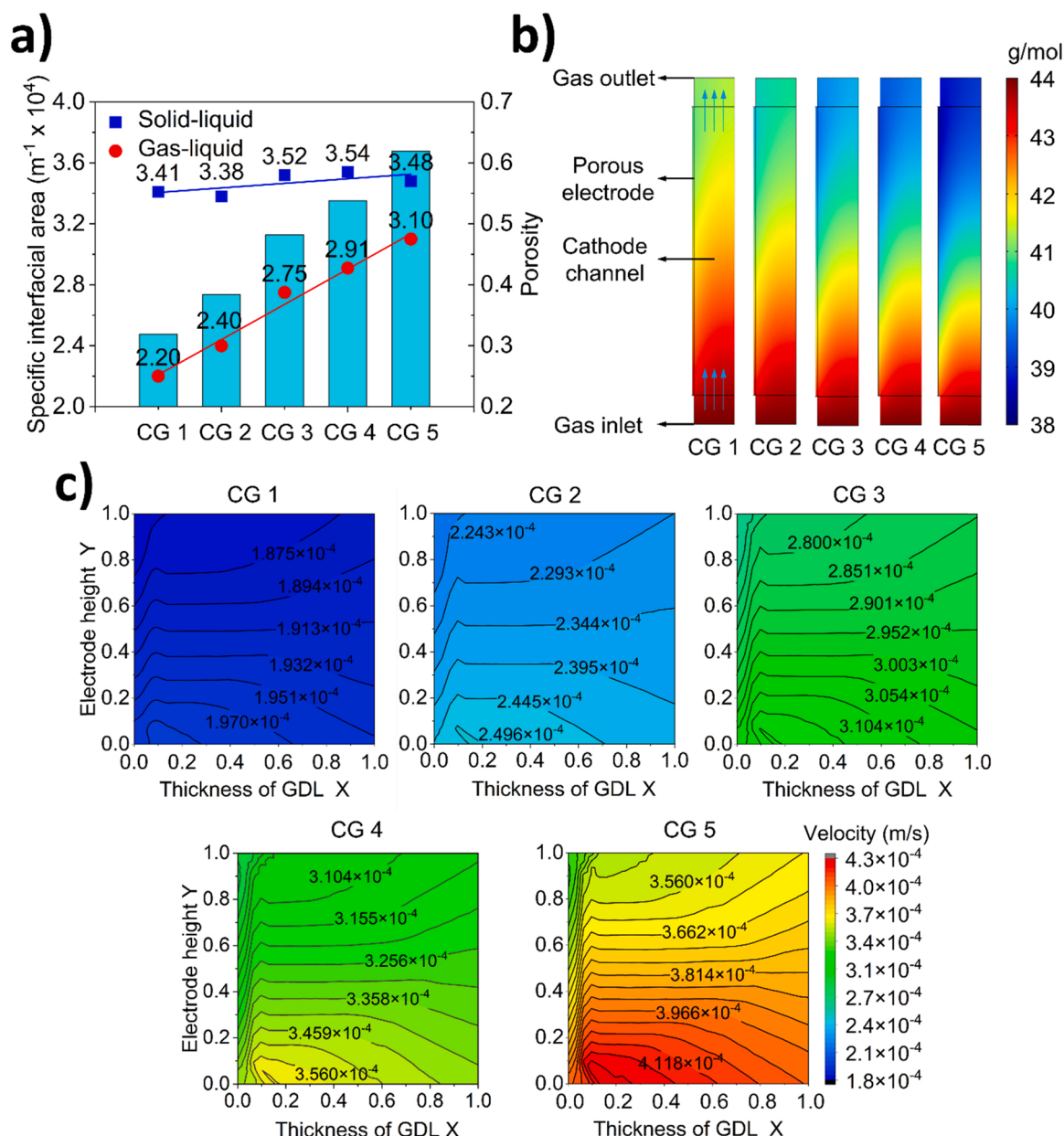


**Fig. 4.** a) Specific interfacial area of CG catalysts layer (line-plot correspond to specific interfacial area, and the column plot correspond to porosity). b) Mean molar mass in CG, GDL, CL at  $-1.0$  V vs. RHE, where the upper and bottom boxes represent the outlet and inlet of the gas chamber, the cylinder in the middle is the gas chamber. The thin layer attached to GDL on the left side is CL which has different parameters. c) Average CO<sub>2</sub> gas flow velocity in GDL at  $-1.0$  V vs. RHE, where  $X = 0$  for the 'CL-GDL' interface,  $X = 1$  for the 'GDL-gas chamber' interface.  $Y = 0$  for cathode inlet,  $Y = 1$  for cathode outlet.

internal hydrophobicity and prevents electrode flooding by electrolyte. The Cu<sub>2</sub>O-graphene interaction changes the electronic structure [41], and the Cu<sub>2</sub>O particles prevent the HER in graphene, resulting in a 2D surface sufficient for Cu<sub>2</sub>O to distribute and enhance the surface area of the proton-enriched electrode. The combined effects of these factors yield improved eCO<sub>2</sub>RR results.

The eCO<sub>2</sub>RR was performed at moderate pH to study the effect of electrolyte alkalinity in aqueous electrochemical CO<sub>2</sub> reduction using CG catalysts (Fig. S6). Within the potential range from  $-0.4$  V to  $-1.2$  V vs. RHE, the FE and current density of carbonaceous products increase from CG1 to CG5, aligning well with the 1 M KOH electrolyte results. The CG5 with nanoflower-shaped structure (Fig. S6e) exhibits the FE of 53.11%, 63.90%, 70.12%, 72.72% and 71.82% at  $-0.4$  V,  $-0.6$  V,  $-0.8$  V,  $-1.0$  V, and  $-1.2$  V vs. RHE, respectively. The FEs of Cu<sub>2</sub>O (Fig. S6f) at potentials of  $-0.4$  V,  $-0.6$  V,  $-0.8$  V,  $-1.0$  V, and  $-1.2$  V vs. RHE are 21.56%, 34.31%, 47.87%, 52.90% and 54.71%,

respectively.

Owing to the increase in surface area and porosity, the FE and current density of the carbonaceous products increases from CG2 through CG3 to CG4 (Fig. S6b–d). The current density and FE of carbonaceous products for 1 M KHCO<sub>3</sub> were lower than 1 M KOH. The strong base electrode suppresses HER and promotes eCO<sub>2</sub>RR [22]. The results in 1 M KHCO<sub>3</sub> confirm that the eCO<sub>2</sub>RR can be enhanced using catalysts with higher active sites and a porous structure. The detailed data and relevant random errors are listed in Tables S11–S18. The simulation can be applied to any reaction regardless of the electrolyte.

#### 3.4. Stability evaluation of CG catalysts in GDE cell

The stability of the eCO<sub>2</sub>RR reaction system is essential for commercial implementation because the GDLs may lose their hydrophobicity and permeate by electrolyte after a long-term reaction [42]. The



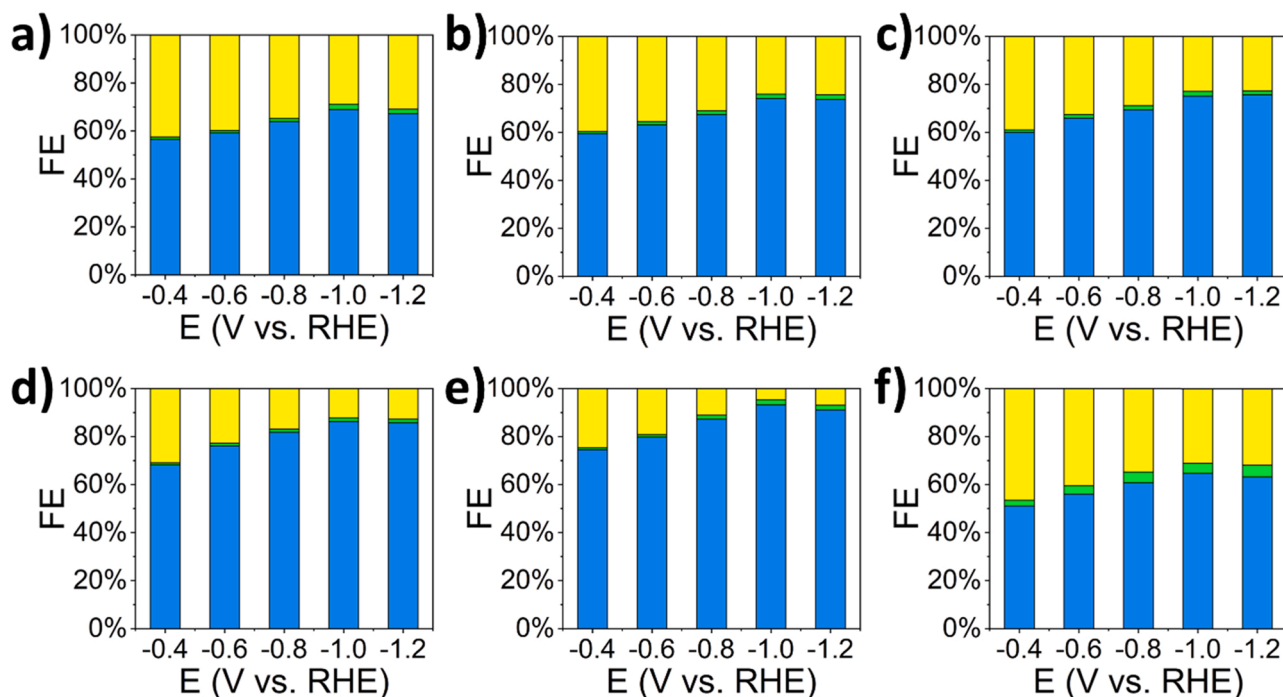


**Fig. 5.** Faradaic efficiency profiles of a-e) CGs1-5 and f) Cu<sub>2</sub>O in 1 M KOH electrolyte for eCO<sub>2</sub>RR with products including CO (blue), formate (green), and H<sub>2</sub> (yellow). (For interpretation of the references to colour in this figure legend, the reader is referred to the web version of this article.)

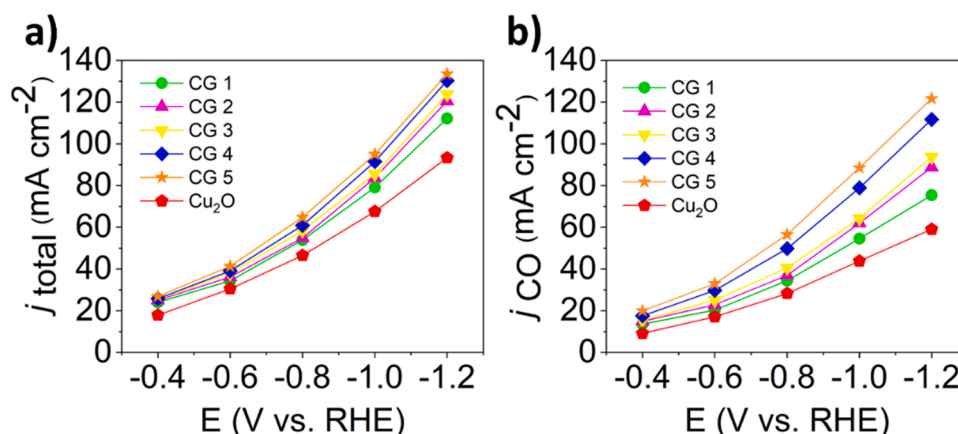


**Fig. 6.** a) Total current density and b) current density of CO for CGs1-5 and Cu<sub>2</sub>O in 1 M KOH electrolyte.

CG catalysts retain good FE of CO (Fig. 7) after the 4-h and 8-h tests compared to the half-hour reaction (Fig. 7a, detailed data and relevant random error are listed in Tables S19 and S20). The current remains stable after 8 h, and the FE values of CO for CGs1-5 after 8 h of reaction were 64.30%, 69.26%, 70.69%, 82.23%, and 88.69%, respectively. The hydrophobic porous CG catalyst layer prevents electrolyte penetration during the reaction. The increase in thickness of the hydrophobic layer from CGs1-5 reduces the electrolyte permeation through the GDL. The enhanced porosity of the catalyst layer increases the gas-liquid-solid (CO<sub>2</sub>-electrolyte-catalyst) interface, which enhances the active sites for eCO<sub>2</sub>RR. Conversely, the FEs decreased significantly after 8 h of reaction using Cu<sub>2</sub>O, and the corresponding FE of CO is 26.91%. Additionally, the CA plot becomes unstable due to electrode permeation. To further explore the reason for the stability of the CG catalysts, we scanned the CG5 electrodes using SEM after the reaction (Fig. 7c). The CG retains the nanoflower shape, even though the outer layers fall on the graphene sheets. Therefore, the catalyst retains a high surface area for the reaction. Cu<sub>2</sub>O nanoparticles exhibited a reduced FE due to the damage of

the catalyst surface (Fig. S7) owing to the electrochemical corrosion, which reduces the number of active sites on its surface and reduces the eCO<sub>2</sub>RR performance.

Impedance spectroscopy was performed on CG catalysts and Cu<sub>2</sub>O cubic catalyst at 0.1 V vs. RHE to study the charge transfer of the CG catalysts (Fig. 7d). The Nyquist plots indicate an increasing trend for all the CG catalysts with the blooming process. The increase in porosity of the catalysts improves the internal charge transfer, which results in enhanced eCO<sub>2</sub>RR performance. In contrast, the Cu<sub>2</sub>O exhibited higher internal resistance, leading to a lower current density for the eCO<sub>2</sub>RR.

#### 4. Conclusions

We developed an architecture-controlled catalyst for the electrochemical conversion of CO<sub>2</sub> to CO. The temperature-dependent CG catalysts with controllable morphologies enhance the eCO<sub>2</sub>RR activity and efficiency by enhancing the gas-liquid and liquid-solid specific areas and the porosity of the catalyst layer. Increasing the concentration of the



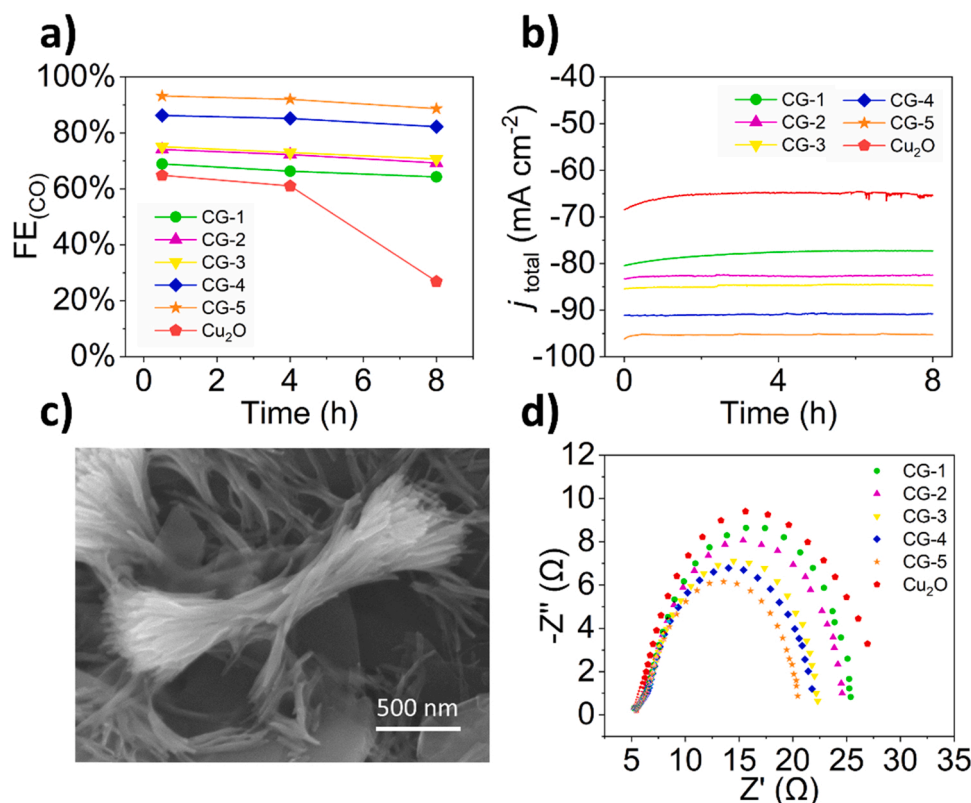


**Fig. 7.** a) FE<sub>CO</sub> results of stability test after 0.5 h, 4 h, and 8 h reaction of the CG catalysts at  $-1.0$  V vs. RHE. b) Stability tests of CGs1–5 and Cu<sub>2</sub>O at  $-1.0$  V vs. RHE for 8 h in 1 M KOH, GDE system. c) SEM image of CG5 after 8 h reaction. d) Electrochemical impedance spectroscopy of CG catalysts and Cu<sub>2</sub>O in 1 M KOH.

incoming CO<sub>2</sub> near the catalyst layer surface increased the CO<sub>2</sub> concentration within the catalyst layer and enhanced the CO<sub>2</sub> velocity in the gas chamber, thereby improving the eCO<sub>2</sub>RR. The enhanced hydrophobicity of the catalyst layer provided considerable stability to the eCO<sub>2</sub>RR system. FE higher than 90% for CO and formate was obtained for CG5 catalyst at  $-1.0$  V vs. RHE in a 1 M KOH electrolyte. The highly porous catalyst layer is hydrophobic and prevents the GDL from being flooded, thereby enhancing the stability with a low FE drop after 8 h of reaction. The enhanced conductivity and active sites of CG5 promote the reaction activity at a current density of  $133.5 \text{ mA cm}^{-2}$  and applied potential of  $-1.2$  V vs. RHE.

Although the catalyst did not form the desired nano-bud or nano-flower structure at temperatures below  $70^\circ\text{C}$  and above  $90^\circ\text{C}$  from the experimental aspect, this study has established a theoretical analysis of the relationship between the CL intensity/mass transfer and the induced eCO<sub>2</sub>RR performance.

#### CRediT authorship contribution statement

**Yucheng Wang:** Investigation, Methodology, Data curation, Figure draw, Writing – review & editing, Writing – original draft. **Hanhui Lei:** Methodology, Simulation, Data curation, Figure draw. **Shun Lu:** XPS characterisation and analysis. **Ziming Yang:** Simulation, Data curation. **Ben Bin Xu:** Co-supervision, Formal analysis. **Lei Xing:** Supervision, Simulation, Methodology, Formal analysis, Writing – review & editing. **Terence Xiaoteng Liu:** Supervision, Software, Methodology, Conceptualization, Writing – review & editing, Project administration, Funding acquisition.

#### Declaration of Competing Interest

The authors declare that they have no known competing financial interests or personal relationships that could have appeared to influence

the work reported in this paper.

#### Acknowledgements

This work was supported by the UK Engineering Physics and Science Research Council (Grant No. EP/S032886/1), and the Royal Society International Exchanges Award (Grant No. IEC\NSFC\201008).

#### Appendix A. Supporting information

Supplementary data associated with this article can be found in the online version at [doi:10.1016/j.apcatb.2021.121022](https://doi.org/10.1016/j.apcatb.2021.121022).

#### References

- [1] T. Wilberforce, A. Olabi, E.T. Sayed, K. Elsaid, M.A. Abdelkareem, Progress in carbon capture technologies, *Sci. Total Environ.* 761 (2020), 143203.
- [2] A.I. Osman, M. Hefny, M. Abdel Maksoud, A.M. Elgarahy, D.W. Rooney, Recent advances in carbon capture storage and utilisation technologies: a review, *Environ. Chem. Lett.* 19 (2021) 797–849.
- [3] P. Renforth, The negative emission potential of alkaline materials, *Nat. Commun.* 10 (2019) 1–8.
- [4] L. Xing, R.C. Darton, A. Yang, Enhanced weathering to capture atmospheric carbon dioxide: modeling of a trickle-bed reactor, *AIChE J.* 67 (2021), e17202.
- [5] J. Fu, K. Jiang, X. Qiu, J. Yu, M. Liu, Product selectivity of photocatalytic CO<sub>2</sub> reduction reactions, *Mater. Today* 32 (2020) 222–243.
- [6] G. Zhao, X. Huang, X. Wang, X. Wang, Progress in catalyst exploration for heterogeneous CO<sub>2</sub> reduction and utilization: a critical review, *J. Mater. Chem. A* 5 (2017) 21625–21649.
- [7] J. Qiao, Y. Liu, F. Hong, J. Zhang, A review of catalysts for the electroreduction of carbon dioxide to produce low-carbon fuels, *Chem. Soc. Rev.* 43 (2014) 631–675.
- [8] D.D. Zhu, J.L. Liu, S.Z. Qiao, Recent advances in inorganic heterogeneous electrocatalysts for reduction of carbon dioxide, *Adv. Mater.* 28 (2016) 3423–3452.
- [9] Y. Zheng, A. Vasileff, X. Zhou, Y. Jiao, M. Jaroniec, S.-Z. Qiao, Understanding the roadmap for electrochemical reduction of CO<sub>2</sub> to multi-carbon oxygenates and hydrocarbons on copper-based catalysts, *J. Am. Chem. Soc.* 141 (2019) 7646–7659.
- [10] S. Liang, N. Altaf, L. Huang, Y. Gao, Q. Wang, Electrolytic cell design for electrochemical CO<sub>2</sub> reduction, *J. CO<sub>2</sub> Util.* 35 (2020) 90–105.

- [11] D.C. Grills, Y. Matsubara, Y. Kuwahara, S.R. Golisz, D.A. Kurtz, B.A. Mello, Electrocatalytic CO<sub>2</sub> reduction with a homogeneous catalyst in ionic liquid: high catalytic activity at low overpotential, *J. Phys. Chem. Lett.* 5 (2014) 2033–2038.
- [12] H.A. Hansen, J.B. Varley, A.A. Peterson, J.K. Norskov, Understanding trends in the electrocatalytic activity of metals and enzymes for CO<sub>2</sub> reduction to CO, *J. Phys. Chem. Lett.* 4 (2013) 388–392.
- [13] S. Nitopi, E. Bertheussen, S.B. Scott, X. Liu, A.K. Engstfeld, S. Horch, B. Seger, I. E. Stephens, K. Chan, C. Hahn, Progress and perspectives of electrochemical CO<sub>2</sub> reduction on copper in aqueous electrolyte, *Chem. Rev.* 119 (2019) 7610–7672.
- [14] T. Hatsukade, K.P. Kuhl, E.R. Cave, D.N. Abram, T.F. Jaramillo, Insights into the electrocatalytic reduction of CO(2) on metallic silver surfaces, *Phys. Chem. Chem. Phys.* 16 (2014) 13814–13819.
- [15] W. Zhang, Y. Hu, L. Ma, G. Zhu, Y. Wang, X. Xue, R. Chen, S. Yang, Z. Jin, Progress and perspective of electrocatalytic CO<sub>2</sub> reduction for renewable carbonaceous fuels and chemicals, *Adv. Sci.* 5 (2018), 1700275.
- [16] R. Francke, B. Schille, M. Roemelt, Homogeneously catalyzed electroreduction of carbon dioxide-methods, mechanisms, and catalysts, *Chem. Rev.* 118 (2018) 4631–4701.
- [17] C.-H. Huang, C.-S. Tan, A review: CO<sub>2</sub> utilization, *Aerosol Air Qual. Res.* 14 (2013) 480–499.
- [18] X. Xiaoding, J. Mouljin, Mitigation of CO<sub>2</sub> by chemical conversion: plausible chemical reactions and promising products, *Energy Fuels* 10 (1996) 305–325.
- [19] C.M. Gabardo, C.P. O'Brien, J.P. Edwards, C. McCallum, Y. Xu, C.-T. Dinh, J. Li, E. H. Sargent, D. Sinton, Continuous carbon dioxide electroreduction to concentrated multi-carbon products using a membrane electrode assembly, *Joule* 3 (2019) 2777–2791.
- [20] J. Durst, A. Rudnev, A. Dutta, Y. Fu, J. Herranz, V. Kalignedi, A. Kuzume, A. A. Permyakova, Y. Paratcha, P. Broekmann, Electrochemical CO<sub>2</sub> reduction – a critical view on fundamentals, materials and applications, *CHIMIA Int. J. Chem.* 69 (2015) 769–776.
- [21] T. Zheng, K. Jiang, N. Ta, Y. Hu, J. Zeng, J. Liu, H. Wang, Large-scale and highly selective CO<sub>2</sub> electrocatalytic reduction on nickel single-atom catalyst, *Joule* 3 (2019) 265–278.
- [22] H. Xiang, S. Rasul, K. Scott, J. Portoles, P. Cumpson, H.Y. Eileen, Enhanced selectivity of carbonaceous products from electrochemical reduction of CO<sub>2</sub> in aqueous media, *J. CO<sub>2</sub> Util.* 30 (2019) 214–221.
- [23] Y. Peng, T. Wu, L. Sun, J.M.V. Nsanzimana, A.C. Fisher, X. Wang, Selective electrochemical reduction of CO<sub>2</sub> to ethylene on nanopores-modified copper electrodes in aqueous solution, *ACS Appl. Mater. Interfaces* 9 (2017) 32782–32789.
- [24] Y. Fu, Y. Li, X. Zhang, Y. Liu, J. Qiao, J. Zhang, D.P. Wilkinson, Novel hierarchical SnO<sub>2</sub> 2 microsphere catalyst coated on gas diffusion electrode for enhancing energy efficiency of CO<sub>2</sub> reduction to formate fuel, *Appl. Energy* 175 (2016) 536–544.
- [25] N. Nilius, H. Fedderwitz, B. Gross, C. Noguera, J. Goniakowski, Incorrect DFT-GGA predictions of the stability of non-stoichiometric/polar dielectric surfaces: the case of Cu<sub>2</sub>O(111), *Phys. Chem. Chem. Phys.* 18 (2016) 6729–6733.
- [26] G.H. Jeong, Y.C. Tan, J.T. Song, G.-Y. Lee, H.J. Lee, J. Lim, H.Y. Jeong, S. Won, J. Oh, S.O. Kim, Synthetic multiscale design of nanostructured Ni single atom catalyst for superior CO<sub>2</sub> electroreduction, *Chem. Eng. J.* 426 (2021), 131063.
- [27] W. Zhang, Y. Hu, L. Ma, G. Zhu, Y. Wang, X. Xue, R. Chen, S. Yang, Z. Jin, Progress and perspective of electrocatalytic CO<sub>2</sub> reduction for renewable carbonaceous fuels and chemicals, *Adv. Sci.* 5 (2018), 1700275.
- [28] J. Rosen, G.S. Hutchings, Q. Lu, S. Rivera, Y. Zhou, D.G. Vlachos, F. Jiao, Mechanistic insights into the electrochemical reduction of CO<sub>2</sub> to CO on nanostructured Ag surfaces, *ACS Catal.* 5 (2015) 4293–4299.
- [29] J. Wu, Y. Huang, W. Ye, Y. Li, CO<sub>2</sub> reduction: from the electrochemical to photochemical approach, *Adv. Sci.* 4 (2017), 1700194.
- [30] H. Mistry, A.S. Varela, C.S. Bonifacio, I. Zegkinoglou, I. Sinev, Y.-W. Choi, K. Kisslinger, E.A. Stach, J.C. Yang, P. Strasser, Highly selective plasma-activated copper catalysts for carbon dioxide reduction to ethylene, *Nat. Commun.* 7 (2016) 1–9.
- [31] P. Yang, Z.J. Zhao, X. Chang, R. Mu, S. Zha, G. Zhang, J. Gong, The functionality of surface hydroxy groups on the selectivity and activity of carbon dioxide reduction over cuprous oxide in aqueous solutions, *Angew. Chem.* 130 (2018) 7850–7854.
- [32] H. Rabiee, L. Ge, X. Zhang, S. Hu, M. Li, S. Smart, Z. Zhu, Z. Yuan, Shape-tuned electrodeposition of bismuth-based nanosheets on flow-through hollow fiber gas diffusion electrode for high-efficiency CO<sub>2</sub> reduction to formate, *Appl. Catal. B: Environ.* 286 (2021), 119945.
- [33] W. Zhu, S. Kattel, F. Jiao, J.G. Chen, Shape-controlled CO<sub>2</sub> electrochemical reduction on nanosized Pd hydride cubes and octahedra, *Adv. Energy Mater.* 9 (2019), 1802840.
- [34] C.-T. Dinh, T. Burdyny, M.G. Kibria, A. Seifitokaldani, C.M. Gabardo, F.P.G. De Arquer, A. Kiani, J.P. Edwards, P. De Luna, O.S. Bushuyev, CO<sub>2</sub> electroreduction to ethylene via hydroxide-mediated copper catalysis at an abrupt interface, *Science* 360 (2018) 783–787.
- [35] F.P.G. De Arquer, C.-T. Dinh, A. Ozden, J. Wicks, C. McCallum, A.R. Kirmani, D.-H. Nam, C. Gabardo, A. Seifitokaldani, X. Wang, CO<sub>2</sub> electrolysis to multicarbon products at activities greater than 1 A cm<sup>−2</sup>, *Science* 367 (2020) 661–666.
- [36] Y. Wang, H. Lei, H. Xiang, Y. Fu, C. Xu, Y. Jiang, B.B. Xu, E.H. Yu, C. Gao, T.X. Liu, Porous bilayer electrode guided gas diffusion for enhanced CO<sub>2</sub> electrochemical reduction, *Adv. Energy Sustain. Res.* 2 (2021), 2100083.
- [37] H. Rabiee, X. Zhang, L. Ge, S. Hu, M. Li, S. Smart, Z. Zhu, Z. Yuan, Tuning the product selectivity of the Cu hollow fiber gas diffusion electrode for efficient CO<sub>2</sub> reduction to formate by controlled surface Sn electrodeposition, *ACS Appl. Mater. Interfaces* 12 (2020) 21670–21681.
- [38] Z. Yang, D. Li, L. Xing, H. Xiang, J. Xuan, S. Cheng, E.H. Yu, A. Yang, Modeling and upscaling analysis of gas diffusion electrode-based electrochemical carbon dioxide reduction systems, *ACS Sustain. Chem. Eng.* 9 (2020) 351–361.
- [39] J. Li, Z. Mei, L. Liu, H. Liang, A. Azarov, A. Kuznetsov, Y. Liu, A. Ji, Q. Meng, X. Du, Probing defects in nitrogen-doped Cu<sub>2</sub>O, *Sci. Rep.* 4 (2014) 1–6.
- [40] Z.-Z. Niu, F.-Y. Gao, X.-L. Zhang, P.-P. Yang, R. Liu, L.-P. Chi, Z.-Z. Wu, S. Qin, X. Yu, M.-R. Gao, Hierarchical copper with inherent hydrophobicity mitigates electrode flooding for high-rate CO<sub>2</sub> electroreduction to multicarbon products, *J. Am. Chem. Soc.* 143 (2021) 8011–8021.
- [41] M.B. Ross, P. De Luna, Y. Li, C.-T. Dinh, D. Kim, P. Yang, E.H. Sargent, Designing materials for electrochemical carbon dioxide recycling, *Nat. Catal.* 2 (2019) 648–658.
- [42] J. Park, H. Oh, T. Ha, Y.I. Lee, K. Min, A review of the gas diffusion layer in proton exchange membrane fuel cells: durability and degradation, *Appl. Energy* 155 (2015) 866–880.